Do shallow injection wells contribute to the triggering of the 2020 M5.0 Mentone earthquake in the Delaware Basin, Texas?

Xinyu Tan[1] and Semechah K. Y. Lui[2]

[1]University of Toronto - Mississauga
[2]University of Toronto

November 24, 2022

Abstract

The M5.0 earthquake that occurred in March 2020 near the town of Mentone in the Delaware Basin, Texas, is one of the largest induced earthquakes recorded in the central US. A former study shows that the triggering of this event can be attributed to the nearby deep injection. Interestingly, the shallow injection wells in this region have an injection volume five times larger than that of deep injection wells. In this study, we investigate the role of these shallow injection wells in the triggering of the M5.0 event despite their farther distance from the mainshock. By performing focal mechanism inversion and earthquake relocation, we determine the precise orientation of the south-facing normal fault plane where the mainshock occurred, followed by fully coupled poroelastic stress modeling of the change of Coulomb Failure Stress (ΔCFS) on the fitted fault plane due to the shallow injection in the region. Results show that shallow wells may cause up to 30 kPa of ΔCFS near the mainshock location, dominated by positive poroelastic stress change. Such perturbation surpasses the general triggering threshold of faults that are well aligned with the local stress field and suggests a nonnegligible role of these shallow injection in the triggering of the mainshock. Our study also highlights the effect of rock properties of injection layers on the magnitude and spatial extent of pore pressure and stress perturbations, supporting the importance of detailed geomechanical evaluation of the reservoir when developing relevant operational and safety policies.

Do shallow injection wells contribute to the triggering of the 2020 M5.0 Mentone earthquake in the Delaware Basin, Texas?

Xinyu Tan[1,2] and Semechah K. Y. Lui[1,2]

[1] Department of Chemical and Physical Sciences, University of Toronto, Mississauga, ON, CA,

[2] Department of Earth Sciences, University of Toronto, Toronto, ON, CA

Corresponding author: Xinyu Tan (xy.tan@mail.utoronto.ca)

Key Points:

- The M5 Mentone earthquake occurred on a south-facing normal fault plane with strike and dip of 81 and 52 degrees.
- Modeling shows shallow injection causing substantial poroelastic stress perturbations and promoting the triggering of the mainshock.
- Rock properties of the injection layer can significantly affect the magnitude of coupled pore pressure and stress perturbations.

Abstract

The M5.0 earthquake that occurred in March 2020 near the town of Mentone in the Delaware Basin, Texas, is one of the largest induced earthquakes recorded in the central US. A former study shows that the triggering of this event can be attributed to the nearby deep injection. Interestingly, the shallow injection wells in this region have an injection volume five times larger than that of deep injection wells. In this study, we investigate the role of these shallow injection wells in the triggering of the M5.0 event despite their farther distance from the mainshock. By performing focal mechanism inversion and earthquake relocation, we determine the precise orientation of the south-facing normal fault plane where the mainshock occurred, followed by fully coupled poroelastic stress modeling of the change of Coulomb Failure Stress (ΔCFS) on the fitted fault plane due to the shallow injection in the region. Results show that shallow wells may cause up to 30 kPa of ΔCFS near the mainshock location, dominated by positive poroelastic stress change. Such perturbation surpasses the general triggering threshold of faults that are well aligned with the local stress field and suggests a nonnegligible role of these shallow injection in the triggering of the mainshock. Our study also highlights the effect of rock properties of injection layers on the magnitude and spatial extent of pore pressure and stress perturbations, supporting the importance of detailed geomechanical evaluation of the reservoir when developing relevant operational and safety policies.

1. Introduction

Underground fluid injection, out of various purposes, such as hydraulic fracturing, wastewater disposal, geothermal utilization and carbon sequestration, has caused a dramatic increase of seismicity globally (Ellsworth, 2013; Bao & Eaton, 2016; Keranen & Weingarten, 2018). With the increase of oil and gas activities in the Delaware Basin, Texas, seismicity rate has also increased drastically (Skoumal et al., 2020, 2021; Zhai et al., 2021). Just between 2014 and 2018, 24 $M \geq 3$ earthquakes have occurred in the Delaware Basin, while the number of $M \geq 3$ earthquakes in the previous 25 years combined (1970 – 2014) is only 20 (Skoumal et al., 2020). On March 26, 2020, an M5.0 event occurred near the border of Reeves County and Culberson county (Figure 1), which is one of the largest induced earthquakes to date. For induced events that occur on faults close to injection operations, their activation is typically attributed to the build-up of pore pressure from these neighboring wells (Keranen et al., 2013). However, for the Mentone case, there are only 4 shallow injection wells within 5 km, all with a small cumulative injection volume ($< 6 \times 10^6$ BBLs). Wells with much larger volume are located at distances between 10 km and 25 km (Figure 1). The distance of the nearest fracturing well is even farther (> 40 km), which implies a weak link between hydraulic fracturing operation and the occurrence of the mainshock (Lund Snee & Dvory, 2020).

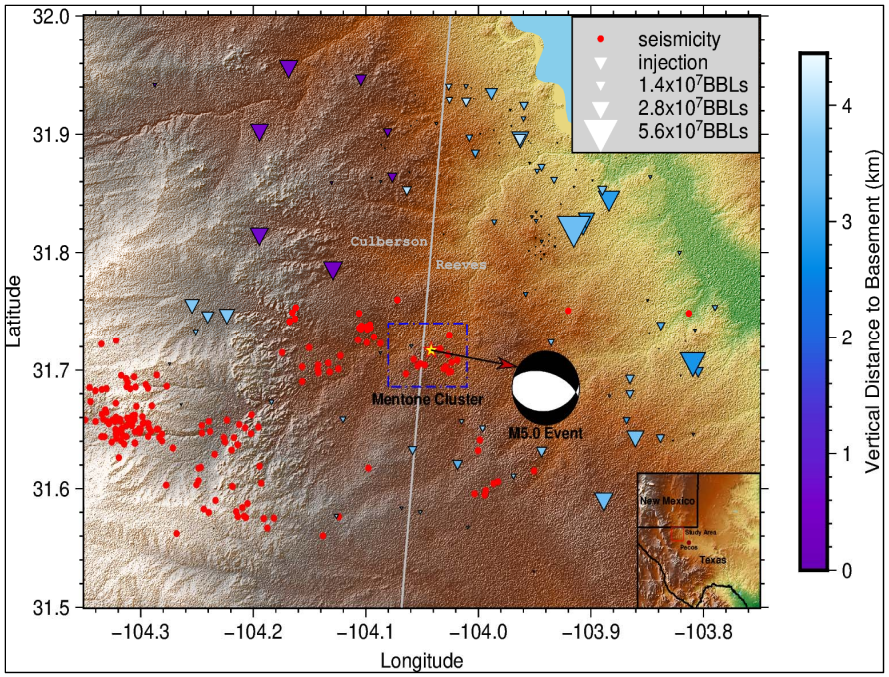

Figure 1. Location of injection wells (inverted triangles) and seismic events (red circles) within 25 km of the mainshock (yellow star). The size and color of the inverted triangles are proportional to the injection volume and the vertical distance between the injection wells and the basement, respectively. Events in the purple dashed rectangle is the Mentone (mainshock) cluster. The bottom-right inset shows the location of the study area in western Texas. Purple inverted triangles are deep injection wells included in the study by Tung et al. (2020).

Previous studies suggested that pore pressure built up through long-distance travel of injected fluid can trigger earthquakes remotely (Keranen et al., 2014; Yeck et al., 2016). In Mentone, Tung et al. (2020) attributed the cause of the M5.0 event to the change of pore pressure in the highly permeable Ellenburger group (limestone layer) due to eight deep injection wells located to the northwest of the mainshock, assuming a hydraulic connection between the limestone layer and the basement. Interestingly, apart from these deep wells, there are also a lot of shallow injection wells within 25 km of the mainshock with much larger total injection volume, approximately five times larger than that of deep injection wells (Figure 2). In particular, the total injection volume of shallow injection wells to the northeast of the mainshock alone have contributed a volume 2.5 times larger than that of the deep injection wells, which is also the largest among the four quadrants around the mainshock. These shallow wells, despite their relatively large epicentral distance (> 5 km), may entertain the possibility of remote triggering from the coupled poroelastic stress due to their high injection volume (Goebel et al., 2017; Goebel & Brodsky, 2018; Zhai et al., 2021). Motivated by this, we investigate in this study the possible contribution of shallow injection wells to the triggering of the M5.0 event. We analyze the contribution from these shallow injection wells to the pore-pressure change and the coupled poroelastic stress on the reactivated fault in the basement, without assuming any hydraulic connection in our model.

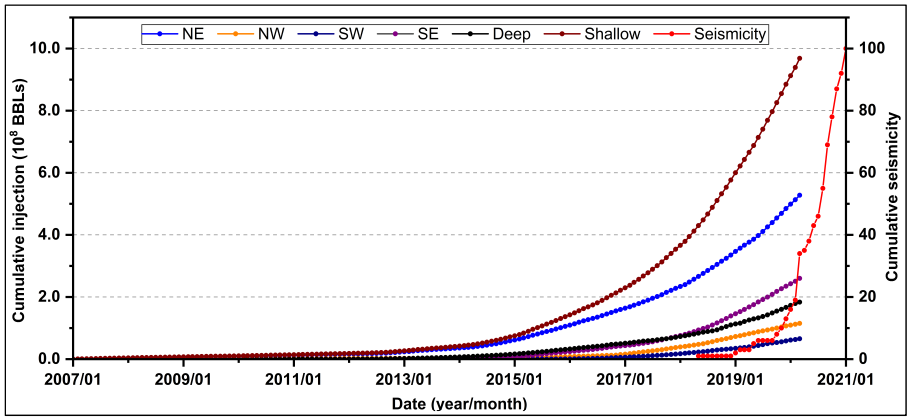

Figure 2. Cumulative seismic activities within 25 km of the mainshock (red graph) and injection volume of five well groups. "NE", "NW", "SW", and "SE" represent cumulative injection volume of shallow wells in the northeast, northwest, southwest, and southeast quadrant, respectively. "Shallow" represents cumulative injection volume of shallow wells within 25 km of the mainshock, "Deep" represents deep injection wells used in Tung et al. (2020).

2. Data and Methods

We analyze the change of the Coulomb failure stress (ΔCFS) on the mainshock fault plane caused by shallow injection wells and explore their roles on the triggering of the M5.0 event. Based on the Coulomb failure theory (Jaeger & Cook, 1979), the value of ΔCFS is defined as:

$$\Delta CFS = \Delta\tau + \mu(\Delta\sigma + \Delta p) \quad (1)$$

where $\Delta\tau$ and $\Delta\sigma$ represent the change of shear stress (positive for promoting failure) and normal stress (positive for unclamping the fault), Δp represents the change of pore pressure on the fault, and μ is the coefficient of friction. The failure is promoted when ΔCFS is positive, and vice versa. From equation (1), changes in direct pore pressure and the resulting poroelastic stress separately contribute to ΔCFS.

Since the normal stress and shear stress on the fault plane are highly sensitive to the location and orientation of the fault (Deng et al., 2020; Lim et al., 2020), correctly resolving the orientation of

the fault plane is an imperative step in this study. Therefore, we first perform focal mechanism inversion on the mainshock and selected adjacent events considering their time and location proximity to the mainshock. Then we constrain the fault plane orientation by fitting relocated events. Lastly, we conduct fully-coupled poroelastic modeling to calculate ΔCFS on the fitted fault plane and investigate the effects of shallow injection wells on the occurrence of the M5.0 event.

2.1 Focal mechanism inversion

To better constrain focal mechanism and to identify events potentially occurred on the mainshock fault plane, the Cut and Paste (CAP) method (Zhao & Helmberger, 1994) is utilized to perform the focal mechanism inversion. Through matching synthetic and observed waveforms of segmented body and surface waves, the CAP method is capable of resolving the optimal source mechanism by grid-searching the seismic moment (M_0), strike, dip and rake of the target event with minimum misfit. Here we use the frequency-wavenumber method to compute the Green's functions as 1D synthetic waveforms input for the inversion (Zhu & Rivera, 2002). The 1D velocity model used in our inversion is derived jointly from sonic velocity logs of a well in the Delaware Basin (Sheng et al., 2020) and the central United States velocity model (CUS). Details of the model can be found in Figure S1 in Supporting Information S1.

Apart from the small cluster containing the mainshock (the Mentone cluster in Figure 1), there are also some neighboring events located between 5 and 10 km to the west and northwest of the mainshock. To determine whether these events occurred on the mainshock fault plane, we conducted focal mechanism inversion on a total of seven events with $M \geq 3.0$, three of which from the Mentone cluster and the other four from the neighboring clusters (Table 1).

Table 1. Catalog information of selected events obtained from IRIS.

Event	Catalog time	Latitude	Longitude	Magnitude	Focal Depth (km)
01	2020-03-26 15:16:27	31.7168	-104.0419	5.0	9.51
02	2020-03-26 08:52:41	31.7065	-104.0237	3.8	5
03	2020-03-29 01:27:06	31.7029	-104.0288	3.5	5
04	2020-09-18 21:48:27	31.7061	-104.1334	3.5	5
05	2020-10-28 14:07:37	31.7011	-104.1244	3.7	5
06	2020-11-15 15:44:53	31.7349	-104.0986	3.3	5
07	2020-09-03 03:52:27	31.7360	-104.1057	3.0	8.03

2.2 Earthquake relocation

To minimize the uncertainty of earthquake locations and to identify separate faults in the study region, we then relocate these events such that individual fault structures can be delineated, which is conducive to stress and pressure calculation. While many wells within 25 km are to the northeast of the mainshock, most seismicity are located to the opposite end of the mainshock (Figure 1). Here we select earthquakes between 225° and 325° to the mainshock for the hypoDD relocation (Waldhauser & Ellsworth, 2000), which include the Mentone cluster and two other clusters aforementioned (Figure 3).

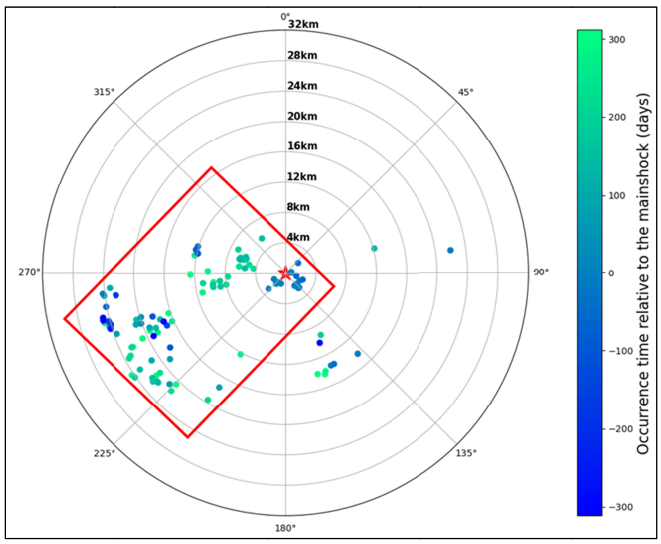

Figure 3. Radial plot displaying events located within 25 km from the mainshock (the red star). Selected events for hypoDD relocation are enclosed within the red rectangle. Colorbar indicates the relative occurrence time of earthquakes to the mainshock.

To efficiently obtain precise input phase arrival times for hypoDD relocation, we first use the powerful program PhaseNet (Zhu & Beroza, 2019) to generate phase arrival time automatically. An example of phase pick output from PhaseNet is included in Figure S2 in Supporting Information S1. To better constrain the accuracy of relocation result, we calculate the cross correlation of data with ObsPy's cross-correlation pick correction function following Deichmann & Fernandez (1992). Data with correlations coefficient > 0.75 is then selected for hypoDD relocation. Parameters used are listed in Table S1 in Supporting Information S1.

2.3 Pressure and stress calculation

To calculate the temporal change of pore pressure and poroealstic stress caused by injection on the fault plane, we adopt the open-source package POEL, a semi-analytical method governed by the following equations (Wang & Kümpel, 2003):

$$(\lambda + 2\mu)\,\nabla(\nabla \cdot \mathbf{u}) - \mu\nabla \times (\nabla \times \mathbf{u}) - \alpha\nabla p = \mathbf{f}(\mathbf{x}, \mathrm{t}) \tag{2}$$

$$Q^{-1}\frac{\partial p}{\partial t} + \alpha\frac{\partial}{\partial t}\nabla \cdot \mathbf{u} - \chi\,\nabla^2 p = q(\mathbf{x}, \mathrm{t}) \tag{3}$$

Where λ and μ are the Lamé parameters, $\mathbf{u}$ is the displacement vector, α is the Biot's coefficient of effective stress, p is pore pressure, $\mathbf{f}(\mathbf{x}, \mathrm{t})$ is the body force on the rock matrix, Q^{-1} is bulk compressibility, χ is hydraulic conductivity, and $q(\mathbf{x}, \mathrm{t})$ is the injection source. Both $\mathbf{f}(\mathbf{x}, \mathrm{t})$ and $q(\mathbf{x}, \mathrm{t})$ are functions of space ($\mathbf{x}$) and time (t). Equation (2) depicts the solid deformation coupled with the change of pore pressure due to fluid injection, which is the fluid-solid coupling. Equation (3) depicts the fluid mass conservation coupled from the solid deformation, which is the solid-fluid coupling (Chang & Segall, 2016; Zhai et al., 2021).

166 Through utilizing the analytical solution from Rudnicki (1986) for equation (2) and (3) in the
167 homogeneous whole space, POEL models the pore pressure and strain tensor of rock matrix
168 caused by time-varying injection in a cylindrically symmetrical layered poroelastic half-space
169 (schematic illustration shown in Figure 4).

170

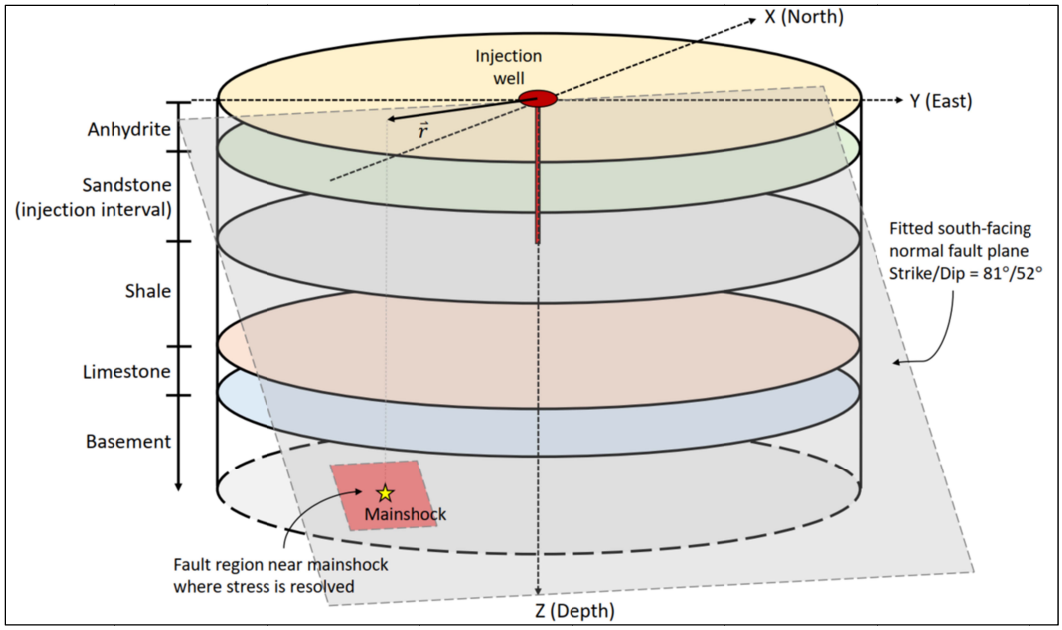

171

172 **Figure 4.** Schematic illustration of simulation domain in POEL (dimensions not to scale). Our
173 model comprises of five geologic layers, with injection occurring within the sandstone layer.
174 Coulomb failure stresses are calculated on the fitted fault plane near the mainshock location.

175

176 In our simulation, the boundary-value-problem mode is chosen which describes the scenario with
177 fluid injected into a system, assuming an initial pore pressure of 0 MPa (Barbour et al., 2017).
178 The input geomechanical parameters are shear modulus μ, Poisson's ratio ν of drained condition
179 and ν_u of undrained condition, Skempton coefficient B and hydraulic diffusivity D. Other
180 poroelastic parameters including λ, α, Q^{-1} and χ can be obtained with these five input
181 parameters (Wang & Kümpel, 2003; Barbour et al., 2017):

182 $$\lambda = \frac{2\nu\mu}{1-2\nu} \quad (4)$$

$$\alpha = \frac{3(\nu_u - \nu)}{(1-2\nu)(1+\nu_u)B} \quad (5)$$

$$Q^{-1} = \frac{9}{2}\frac{(1-2\nu_u)(\nu_u - \nu)}{(1-2\nu)(1+\nu_u)^2\mu B^2} \quad (6)$$

$$\chi = \frac{9}{2}\frac{(1-\nu_u)(\nu_u - \nu)D}{(1-\nu)(1+\nu_u)^2\mu B^2} \quad (7)$$

The geological model implemented in Tung et al. (2020) is composed of five layers: (from top to bottom) anhydrite, sandstone, shale, limestone, and basement. According to the depth distribution of injection wells within 25 km of the mainshock (Figure S3 in Supporting Information S1), we make slight modifications to the thickness of these layers such that all the shallow and deep injections occur in the high permeable sandstone and limestone layers, respectively. Furthermore, we adjust the conductivity of two layers (anhydrite/halite and shale) and the Skempton coefficient of the shale layer based on relevant studies (Beauheim & Roberts, 2002; Makhnenko et al., 2011; Suarez-Rivera & Fjær, 2013; Li et al., 2020; Zhai et al., 2021). Parameters of the modified geological model are listed in Table 2. Based on the pore pressure and strain tensor of the rock matrix modeled from POEL, we then perform tensor transformation to obtain the local pore pressure, normal stress and shear stress on the fault plane where the mainshock occurred (Zoback, 2010; Figure 4).

Table 2. Geological model used in our analysis (modified from Tung et al., 2020).

Rock type	Depth (m)	μ (Pa)	ν	ν_u	B	D (m^2s^{-1})
Anhydrite, halite	0 - 700	5.96E+09	0.26	0.40	0.86	0.00002
Sandstone	700 - 2500	26.91E+09	0.26	0.36	0.58	0.64000
Shale	2500 - 4500	26.91E+09	0.26	0.37	0.60	0.00002
Limestone	4500 - 5200	12.10E+09	0.26	0.36	0.65	1.00000
Basement	5200 -	30.86E+09	0.26	0.33	0.80	0.00002

3. Results

3.1 Focal mechanism inversion and earthquake cluster relocation

Focal mechanism inversion parameters and results are listed in Table 3. Figure 5 shows the cross-correlation between synthetic and observed waveforms of the M5.0 event at the optimal depth, and the relative misfit error at different focal depths. Inversion results of other selected events are in Figures S4 – S9 in Supporting Information S1. Our results show that events 01, 02 and 03 share similar focal mechanisms, which are different from that of events 04 and 05, and events 06 and 07. It implies that events 04-07 are likely from two other neighboring clusters that occurred on different fault planes with the consideration of the time and location of the Mentone cluster (Figure 1).

Table 3. Parameters used in the CAP inversion and inverted focal mechanisms. Time windows for Pnl and S wave segments used in CAP are 35s and 70s, respectively.

Event	Filtered frequency range (Hz)		Focal Mechanism from CAP (strike, dip,rake)		Optimal depth (km)
	Pnl waves	S waves			
01	0.02-0.10	0.02-0.10	288°, 51°, -67°	74°, 44°, -115°	6.6
02	0.05-0.20	0.05-0.20	280°, 49°, -58°	56°, 50°, -121°	5.4
03	0.10-0.20	0.10-0.20	299°, 40°, -46°	67°, 62°, -120°	5.4
04	0.12-0.22	0.10-0.20	322°, 39°, -35°	80°, 68°, -123°	5.4
05	0.12-0.22	0.10-0.20	323°, 43°, -42°	86°, 62°, -124°	5.4
06	0.12-0.25	0.15-0.30	17°, 57°, -15°	115°, 77°, -146°	3.3
07	0.08-0.22	0.10-0.25	10°, 66°, -14°	105°, 77°, -155°	5.1

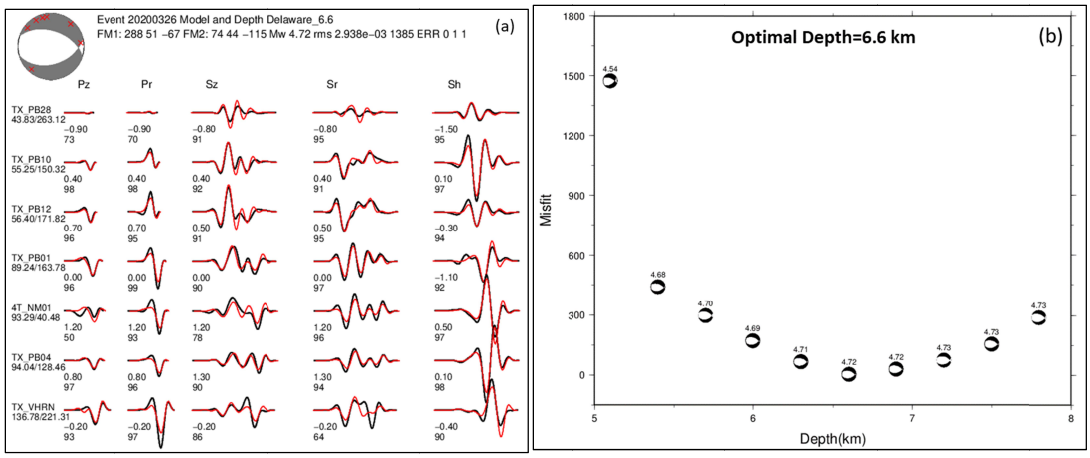

Figure 5. (a) Synthetic (red) and recorded (black) waveform have the highest correlation at the optimal depth of 6.6 km for the M5.0 event. The numbers below the waveforms are optimal shift time (in second) and cross correlation, respectively. (b) Relative misfit error of the mainshock inversion at different focal depths.

Similar to focal mechanism inversion results, earthquake relocation analysis also indicates three separate earthquake clusters. Compared with catalog locations, relocated events within each cluster are positioned more closely to one another (Figure 6). Based on hypoDD results, the orientations of the respective fault planes can be approximated in 3D (Figure 7). The fitted strike/dip angles of clusters *a*, *b* and *c* are 81°/52°, 95°/58°, and 113°/73°, respectively. Although these three clusters share similar dip angles, there is obvious disparity among their strike angles. The fitted fault plane of cluster *a* is regarded as the fault plane on which the mainshock occurred and ΔCFS is evaluated.

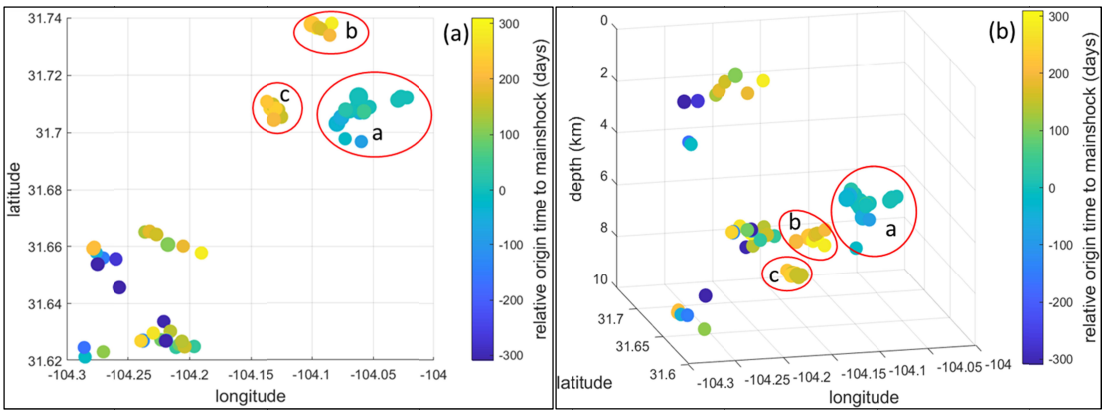

Figure 6. (a-b) 2D and 3D view of the relocated events, respectively. Colorbar represents their event time relative to that of the mainshock. Clusters *a*, *b* and *c* are circled in red.

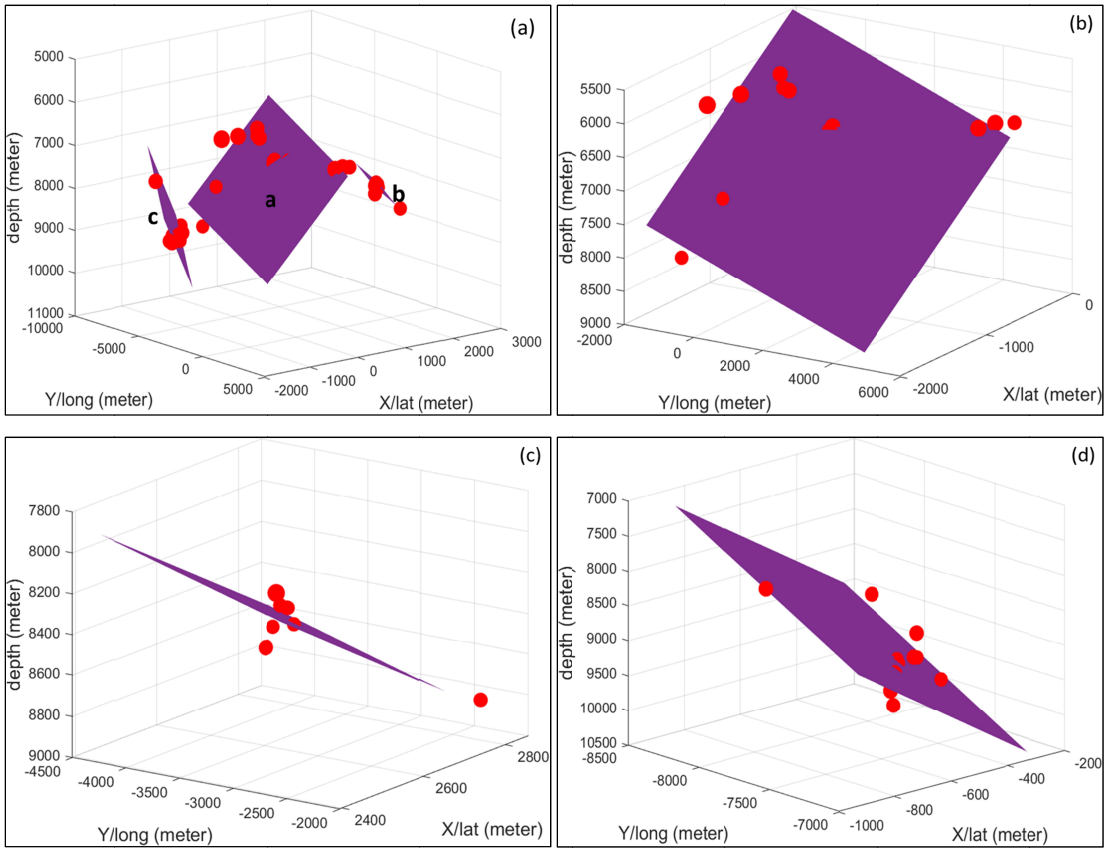

Figure 7. (a) Fitted fault planes of clusters *a*, *b* and *c* based on hypoDD results. (b)-(d) Zoomed-in plots of individual clusters *a*, *b*, and *c*, and their corresponding fitted planes.

3.2 Fully-coupled poroelastic stress modeling

To perform the fully coupled poroelastic stress modeling, we select wells within 25 km of the mainshock with relatively large injection volume and divide them into four groups based on their positions from the mainshock, i.e. the northeast, southeast, southwest and northwest quadrants. The selected wells account for about 69%, 40.7%, 59.8% and 46.7% of the total injection volume in each respective quadrants. To simplify the calculation process, within each quadrant, we further group injection wells that are close to one another (within about 0.5 km on average) and assign them the same average location. We then calculate the change in pore pressure, normal and shear stress resulted from individual wells on the fitted fault plane (Figure 4) and sum their results to obtain the total normal and shear stress change caused by the shallow wells in the region. Specific information about the selected wells, the resulted pore pressure, normal and shear stress are listed in Table S2 in Supporting Information S1.

The time evolution of the total monthly injection rate of selected wells, as well as the resulted change in pore pressure, normal stress, shear stress, poroelastic stress and ΔCFS are displayed in Figure 8. It is found that at the early stage of the injection (before 2015) with low injection rate, pressure and stress perturbations near the mainshock are pretty small due to the large distance between selected wells and the mainshock (varies between 10 km and 20 km). Starting in 2015, with increasing injection rate, the total pore pressure perturbation near the mainshock transitioned from positive (encourage fault slip) to negative (inhibit fault slip), and the rate of the decrease increases with injection rate. This phenomenon is mainly caused by the coupling effect of the poroelastic stress on the pore pressure. Due to the low permeability of the thick shale layer below the shallow injection sandstone layer, direct pore pressure change due to percolation of injected fluid through the shale layer is unlikely. Instead, the change in pore pressure change is primarily resulted from the coupling effect of poroelastic stress. According to Chang & Segall (2016), injected fluid causes expansion of the layer below the injection layer, which subsequently compacts the layer at further distances. The boundary of expansion and compaction is determined by rock properties and injection parameters, and the zone of expansion gradually moves outward as injection continues. In the beginning, due to low injection rate and large distance between the injection wells and the mainshock, the basement rock layer near the mainshock location underwent compaction and, hence, the change in pore pressure remained

positive until early 2018. As injection continued, the expansion region continued to move outward, and pore pressure eventually transitioned from positive to negative. Both normal and shear stresses increase throughout the entire injection period and they increase more rapidly with the rise of injection rate. The resulting poroelastic stress change reaches about 19 kPa at the time of the mainshock. Since the change in pore pressure change at the mainshock location is negative, the positive ΔCFS was solely from poroelastic effects.

Overall, the ΔCFS increased with an increasing rate and reached about 20 kPa when the mainshock occurred, which surpasses the general threshold of 10 kPa for seismic events to be triggered (Rothert & Shapiro, 2007; Deng et al., 2020). Since the fitted fault plane is well aligned with the local stress field, it is possible that even a small perturbation may reactivate the fault (Lund Snee & Dvory, 2020). Furthermore, rather than considering all the injection wells in this region, only wells with relatively large injection volumes were included in our calculation. Based on the injection volume and locations of all the shallow injection wells in this region, the total ΔCFS from all the shallow injection wells is estimated to be around 30 kPa. As aforementioned, Tung et al. (2020) analyzed the effect of eight deep injection wells in the Ellenburger group (limestone layer) near the mainshock location and obtained a ΔCFS of about 80 kPa, assuming the limestone layer and the basement are hydraulically connected. Without this assumption, the actual ΔCFS in the basement rock could potentially be lower. Therefore, while the ΔCFS from shallow injection appears to be less significant compared to that from deep injection, our result implies that the shallow wells in this region play a nonnegligible role in the triggering of the M5.0 Mentone earthquake, primarily due to poroelastic stress increase.

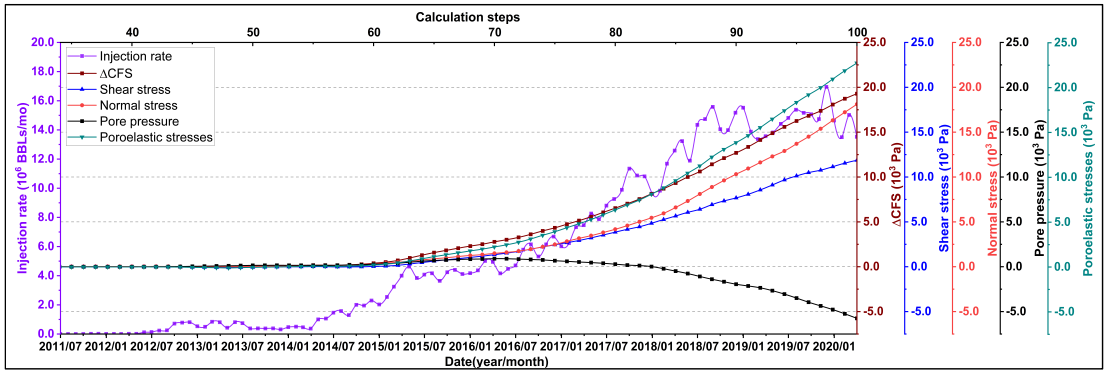

Figure 8. Time evolution of the montly injection rate of selected wells, as well as the change in pore pressure, poroelastic stress, normal stress, shear stress and ΔCFS on the fitted fault plane near the mainshock location until the occurrence of the M5.0 mainshock.

4. Discussion

To establish a detailed comparison of the effects of shallow and deep injection wells, we select two wells with similar total injection volume of 3.0×10^7 BBLS and lateral distance of about 18 km from the mainshock but different injection depths (Table S3 and Figure S10 in Supporting Information S1). The shallow well injects within the sandstone layer, while the deep within the limestone layer. We calculate their resulted ΔCFS at the mainshock location, assuming an isolated sealed fault in the basement with no hydraulic connection to layers above. Interestingly, these two wells cause similar overall ΔCFS of approximately 1 kPa in the basement layer (Figure 9). In particular, at the mainshock location, ΔCFS contributed from shallow injection is approximately 1.3 kPa, which is actually slightly larger than that from deep injection (~0.5 kPa).

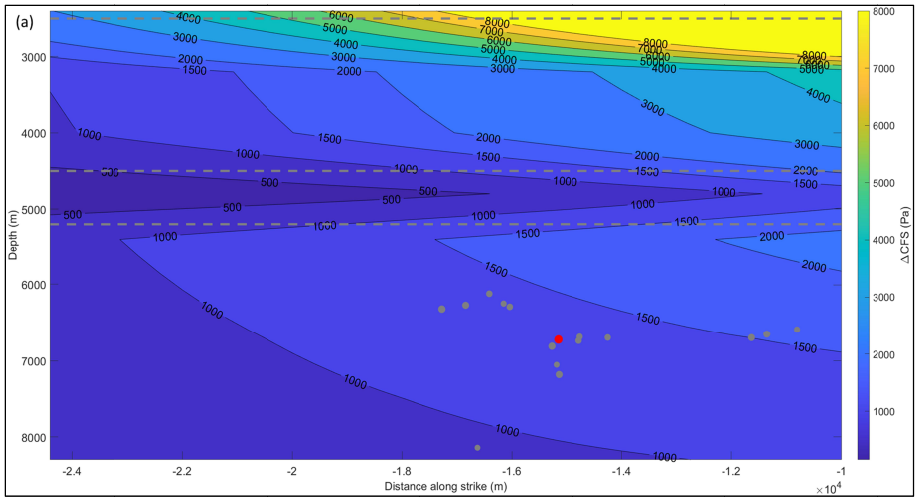

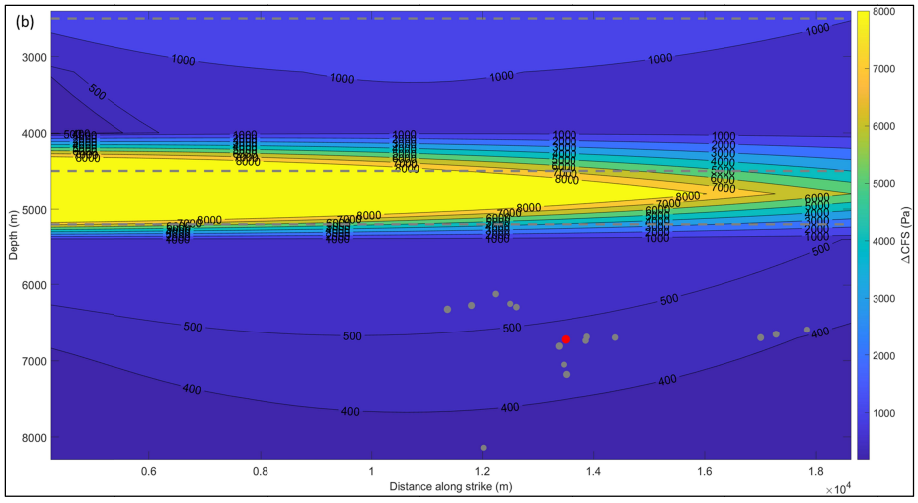

Figure 9. ΔCFS of (a) shallow and (b) deep injection wells. Gray dash lines separate the sandstone, shale, limestone and basement layers (from top to bottom). Red circle denotes mainshock location. Change in pore pressure, normal and shear stress is shown in Figure S11 in Supporting Information S1.

To fully understand how the deep injection results in a smaller ΔCFS, we model another shallow-injection scenario (called SI-2 hereafter) and compare that against the original shallow injection scenario (called SI-1 hereafter), with the sole focus on the rock properties of the injection layer. In SI-1, injection occurs within a sandstone layer. In SI-2, we replace the sandstone layer with a limestone layer, while keeping all other parameters unchanged. Simulation results of SI-2 are displayed in Figure S12 in Supporting Information S1. We find that in SI-2, the resulted pore pressure change in the limestone injection layer is smaller than that in the sandstone injection layer in SI-1. The change in normal stress, shear stress and ΔCFS near the mainshock location are also smaller than those in SI-1. Although the modeling results are numerical solutions in multilayers, the steady-state analytical solutions of injection-induced poroelastic deformation $\mathbf{u}\ (\mathbf{x},\ t)$ and pore pressure $p\ (\mathbf{x},\ t)$ in a whole homogeneous space can provide some insights for these observations, which are fundamental equations used in the POEL package (Rudnicki, 1986; Wang & Kümpel, 2003):

$$\mathbf{u}\ (\mathbf{x},\ t) = \frac{q_o(1+\nu_u)B}{24\pi(1-\nu_u)D}\frac{\mathbf{x}-\mathbf{x_s}}{R} \tag{8}$$

$$p\,(\mathbf{x},\ t) = \frac{q_o}{4\pi\chi}\frac{\mathbf{1}}{R} \tag{9}$$

where $\mathbf{x_s}$ is the position of the injection source, $R = |\mathbf{x} - \mathbf{x_s}|$ is the distance between the injection source and the mainshock, and q_o is a constant injection rate. According to these two equations, $\mathbf{u}$ and p primarily depend on properties of the rock medium. Darcy conductivity $\chi_{limestone}$ and $\chi_{sandstone}$ is about $4.2 \times 10^{-11}\ m^2/(Pa \cdot s)$ and $1.5 \times 10^{-11}\ m^2/(Pa \cdot s)$, respectively, which explains the larger pore pressure change in the sandstone injection layer in SI-1 than in the limestone injection layer in SI-2, according to equation (9). In equation (8), $\left[\frac{(1+\nu_u)B}{(1-\nu_u)D}\right]$ for limestone and sandstone is 1.3812 s/m^2 and 1.9258 s/m^2, respectively, and hence the resulted poroelastic deformation in a sandstone medium is larger than that in a limestone medium. Since SI-1 and SI-2 differs only by the rock type of the injection layer, the overall deformation $\mathbf{u}\,(\mathbf{x},\ t)$ in the basement layer where the mainshock occurs (6.7 km) would also be larger in SI-1 than that in SI-2 (Figure S13 in Supporting Information S1).

We also compare the injection-induced volumetric strain at the mainshock depth of 6.7 km in both scenarios and find that due to the different rock properties, the resulted volumetric strain in SI-1 is much larger than that in SI-2 when wells are less than 20 km from the mainshock (Figure S14 in supporting information). Interestingly, volumetric strain decreases more slowly with distance in SI-2 (limestone), and hence the volumetric strain in SI-1 actually falls below that in SI-2 beyond 20 km. Furthermore, the volumetric strain in SI-1 becomes negative beyond 25 km. This can be explained by the injection-induced deformation transitioning from expansion to compression, and the exact position of this transition is, again, governed by the intrinsic rock properties, as well as the injection parameters (Chang & Segall, 2016).

These modeling results demonstrate that the rock properties of the injection layer as well as the relative location of the injection to the mainshock both significantly influence the resulted poroelastic deformation. It explains the lower value of the ΔCFS of the deep injection in this case, and how the larger ΔCFS from shallow injection is primarily due to substantial coupled poroelastic stress change. In the Delaware Basin, there are a lot of shallow injection wells with large injection volume within 20 km of the mainshock location, and hence our modeling results

suggest that they can cumulatively cause significant poroelastic stress perturbations to the basement faults.

5. Conclusions

In this work, we explored the potential role of shallow injection wells in the triggering of the M5.0 Mentone earthquake in the Delaware basin. Although the injection depth of these wells is pretty shallow and far from basement faults, due to their large injection volume, the cumulative ΔCFS, which is mostly due to poroelastic stress perturbation, surpasses the common threshold of 10 kPa at which critically stressed faults can be triggered. Based on this, it is concluded that the shallow injection in the region did contribute substantially to the triggering of the M5.0 earthquake. Our results confirms the significance of poroelastic stress triggering over large distances, especially when the injection volume is large. Furthermore, our study highlights the effect of rock properties of injection layers in the extent of pressure and stress perturbations caused by fluid injection. In this case, injection in sandstone results in much more prominent stress perturbations than in limestone. Overall, our results have important implications for future injection operations, especially when there exists thick impermeable geologic layers between the injection and basement faults. Due to the cumulative coupled poroelastic stress perturbation over large distances, regulators should account for an extended region near injection sites when developing relevant operational policies.

Acknowledgments

The authors would like to express their sincere thanks to Dr. Rongjiang Wang and Dr. Kai Deng for their helpful discussions. Injection and seismic data are obtained from the Railroad Commission of Texas and Incorporated Research Institutions for Seismology (IRIS), respectively (https://www.rrc.texas.gov/; last accessed January 2021); https://ds.iris.edu/wilber3/find_event; last accessed January 2021). Seismic event catalogue

information is retrieved from and the United States Geological Survey (https://www.usgs.gov/natural-hazards/earthquake-hazards/earthquakes; last access January 2021). This work is supported by the Natural Sciences and Engineering Research Council of Canada (Discovery Grant 2019-06482).

References

Bao, X., & Eaton, D. W. (2016). Fault activation by hydraulic fracturing in western Canada. *Science, 354*(6318), 1406-1409.

Barbour, A. J., Norbeck, J. H., & Rubinstein, J. L. (2017). The effects of varying injection rates in Osage County, Oklahoma, on the 2016 M w 5.8 Pawnee earthquake. *Seismological Research Letters, 88*(4), 1040-1053.

Beauheim, R. L., & Roberts, R. M. (2002). Hydrology and hydraulic properties of a bedded evaporite formation. *Journal of Hydrology, 259*(1-4), 66-88.

Chang, K. W., & Segall, P. (2016). Injection-induced seismicity on basement faults including poroelastic stressing. *Journal of Geophysical Research: Solid Earth, 121*(4), 2708-2726.

Deichmann, N., & Garcia-Fernandez, M. (1992). Rupture geometry from high-precision relative hypocentre locations of microearthquake clusters. *Geophysical Journal International, 110*(3), 501-517.

Deng, K., Liu, Y., & Chen, X. (2020). Correlation between poroelastic stress perturbation and multidisposal wells induced earthquake sequence in Cushing, Oklahoma. *Geophysical Research Letters, 47*(20), e2020GL089366.

Ellsworth, W. L. (2013). Injection-induced earthquakes. *Science*, *341*(6142).

Goebel, T. H. W., Weingarten, M., Chen, X., Haffener, J., & Brodsky, E. E. (2017). The 2016 Mw5. 1 Fairview, Oklahoma earthquakes: Evidence for long-range poroelastic triggering at> 40 km from fluid disposal wells. *Earth and Planetary Science Letters, 472,* 50-61.

Goebel, T. H., & Brodsky, E. E. (2018). The spatial footprint of injection wells in a global compilation of induced earthquake sequences. *Science, 361*(6405), 899-904.

Jaeger, J. C. & N. G. W. Cook (1979). Fundamentals of Rock Mechanics, 3rd ed., Chapman and Hall, London.

Keranen, K. M., Savage, H. M., Abers, G. A., & Cochran, E. S. (2013). Potentially induced earthquakes in Oklahoma, USA: Links between wastewater injection and the 2011 Mw 5.7 earthquake sequence. *Geology*, *41*(6), 699-702.

Keranen, K. M., Weingarten, M., Abers, G. A., Bekins, B. A., & Ge, S. (2014). Sharp increase in central Oklahoma seismicity since 2008 induced by massive wastewater injection. *Science*, *345*(6195), 448-451.

Keranen, K. M., & Weingarten, M. (2018). Induced seismicity. *Annual Review of Earth and Planetary Sciences*, *46*, 149-174.

Li, Z., Ripepi, N., & Chen, C. (2020). Using pressure pulse decay experiments and a novel multi-physics shale transport model to study the role of Klinkenberg effect and effective stress on the apparent permeability of shales. *Journal of Petroleum Science and Engineering, 189,* 107010.

Lim, H., Deng, K., Kim, Y. H., Ree, J. H., Song, T. R., & Kim, K. H. (2020). The 2017 Mw 5.5 Pohang earthquake, South Korea, and poroelastic stress changes associated with fluid injection. *Journal of Geophysical Research: Solid Earth*, *125*(6), e2019JB019134.

Lund Snee, J. E., & Dvory, N. Z. (2020). Magnitude 5.0 earthquake shakes West Texas. jenseriklundsnee. com.

Makhnenko, R. Y., Riedel, J. J., & Labuz, J. F. (2011, June). Undrained plane strain compression of shale. In *45th US Rock Mechanics/Geomechanics Symposium.* OnePetro.

Rothert, E., & Shapiro, S. A. (2007). Statistics of fracture strength and fluid-induced microseismicity. *Journal of Geophysical Research: Solid Earth*, *112*(B4).

Rudnicki, J. W. (1986). Fluid mass sources and point forces in linear elastic diffusive solids. *Mechanics of Materials, 5*(4), 383-393.

454 Sheng, Y., Ellsworth, W. L., & Pepin, K. S. S. (2020, December). On the Depth of Earthquakes
455 in the Delaware Basin-A Case Study along the Reeves-Pecos County line. In *AGU Fall Meeting*
456 *Abstracts* (Vol. 2020, pp. S013-0007).

457

458 Skoumal, R. J., Barbour, A. J., Brudzinski, M. R., Langenkamp, T., & Kaven, J. O. (2020).
459 Induced seismicity in the Delaware basin, Texas. *Journal of Geophysical Research: Solid*
460 *Earth*, *125*(1), e2019JB018558.

461

462 Skoumal, R. J., Kaven, J. O., Barbour, A. J., Wicks, C., Brudzinski, M. R., Cochran, E. S., &
463 Rubinstein, J. L. (2021). The induced Mw 5.0 March 2020 west Texas seismic sequence. *Journal*
464 *of Geophysical Research: Solid Earth*, *126*(1), e2020JB020693.

465

466 Suarez-Rivera, R., & Fjær, E. (2013). Evaluating the poroelastic effect on anisotropic, organic-
467 rich, mudstone systems. *Rock mechanics and rock engineering, 46*(3), 569-580.

468

469 Tung, S., Zhai, G., & Shirzaei, M. (2020). Potential link between 2020 Mentone, West Texas M5
470 earthquake and nearby wastewater injection: implications for aquifer mechanical
471 properties. *Geophysical Research Letters*, 2020GL090551.

472

473 Waldhauser, F., & Ellsworth, W. L. (2000). A double-difference earthquake location algorithm:
474 Method and application to the northern Hayward fault, California. *Bulletin of the seismological*
475 *society of America*, *90*(6), 1353-1368.

476

477 Wang, R., & Kümpel, H. J. (2003). Poroelasticity: Efficient modeling of strongly coupled, slow
478 deformation processes in a multilayered half-space. *Geophysics*, *68*(2), 705-717.

479

480 Yeck, W. L., Weingarten, M., Benz, H. M., McNamara, D. E., Bergman, E. A., Herrmann, R. B.,
481 ... & Earle, P. S. (2016). Far-field pressurization likely caused one of the largest injection
482 induced earthquakes by reactivating a large preexisting basement fault structure. *Geophysical*
483 *Research Letters*, *43*(19), 10-198.

484

485 Zhai, G., Shirzaei, M., & Manga, M. (2021). Widespread deep seismicity in the Delaware Basin,
486 Texas, is mainly driven by shallow wastewater injection. *Proceedings of the National Academy*
487 *of Sciences*, *118*(20).

488

489 Zhao, L. S., & Helmberger, D. V. (1994). Source estimation from broadband regional
490 seismograms. *Bulletin of the Seismological Society of America*, *84*(1), 91-104.

491

Zhu, L., & Rivera, L. A. (2002). A note on the dynamic and static displacements from a point source in multilayered media. *Geophysical Journal International, 148*(3), 619-627.

Zhu, W., & Beroza, G. C. (2019). PhaseNet: a deep-neural-network-based seismic arrival-time picking method. *Geophysical Journal International, 216*(1), 261-273.

Zoback, M. D. (2010). Reservoir geomechanics. Cambridge university press, p. 156.

References from the supporting information

Sheng, Y., Ellsworth, W. L., & Pepin, K. S. S. (2020, December). On the Depth of Earthquakes in the Delaware Basin-A Case Study along the Reeves-Pecos County line. In *AGU Fall Meeting Abstracts* (Vol. 2020, pp. S013-0007).

[Journal of Geophysical Research: Solid Earth]

Supporting Information for

Do shallow injection wells contribute to the triggering of the 2020 M5.0 Mentone earthquake in the Delaware Basin, Texas?

Xinyu Tan[1,2] and Semechah K. Y. Lui[1,2]

[1]Department of Chemical and Physical Sciences, University of Toronto, Mississauga, ON, CA,

[2]Department of Earth Sciences, University of Toronto, Toronto, ON, CA,

Contents of this file

Introduction

The supporting information here includes figures and tables about relevant information and results of the CAP inversion and hypoDD relocation, schematic illustration and results of the injection-induced pore pressure and poroelastic calculation, and the sensitivity analysis based on the real injection history.

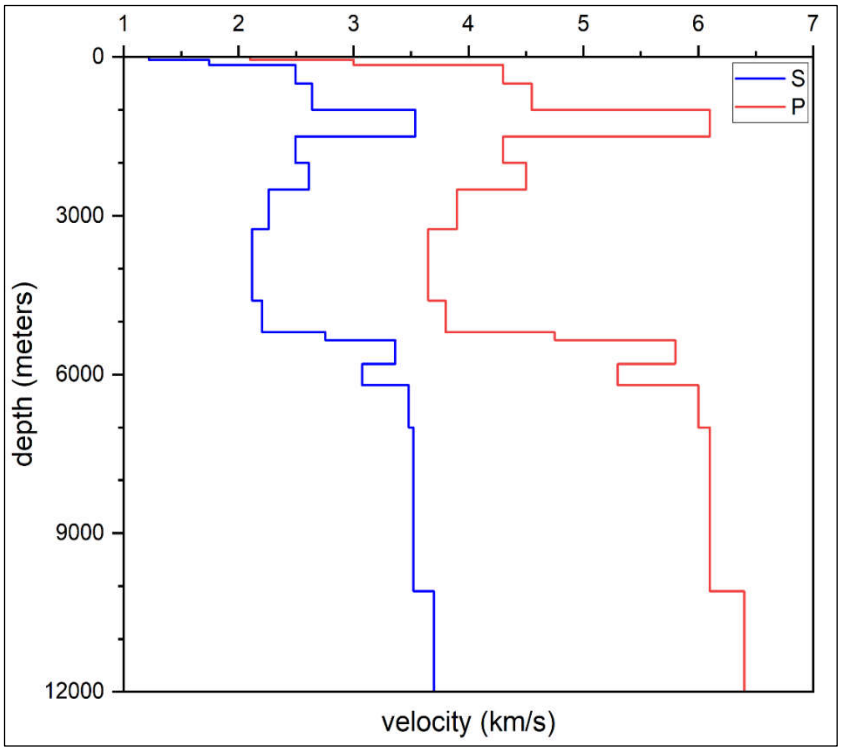

Figure S1. Velocity model used in CAP inversion (modified from Sheng et al., 2020).

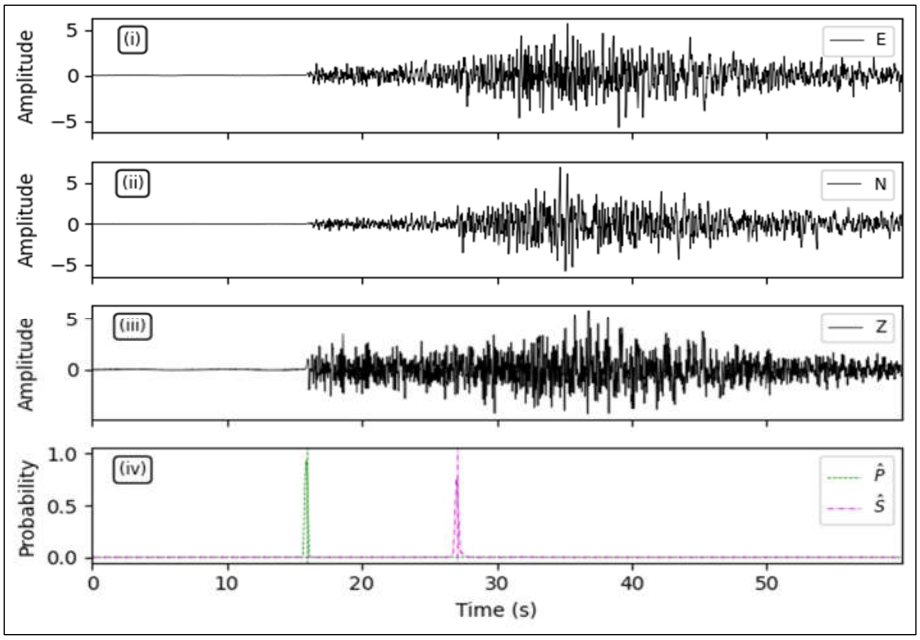

Figure S2. Example of phase pick output from PhaseNet.

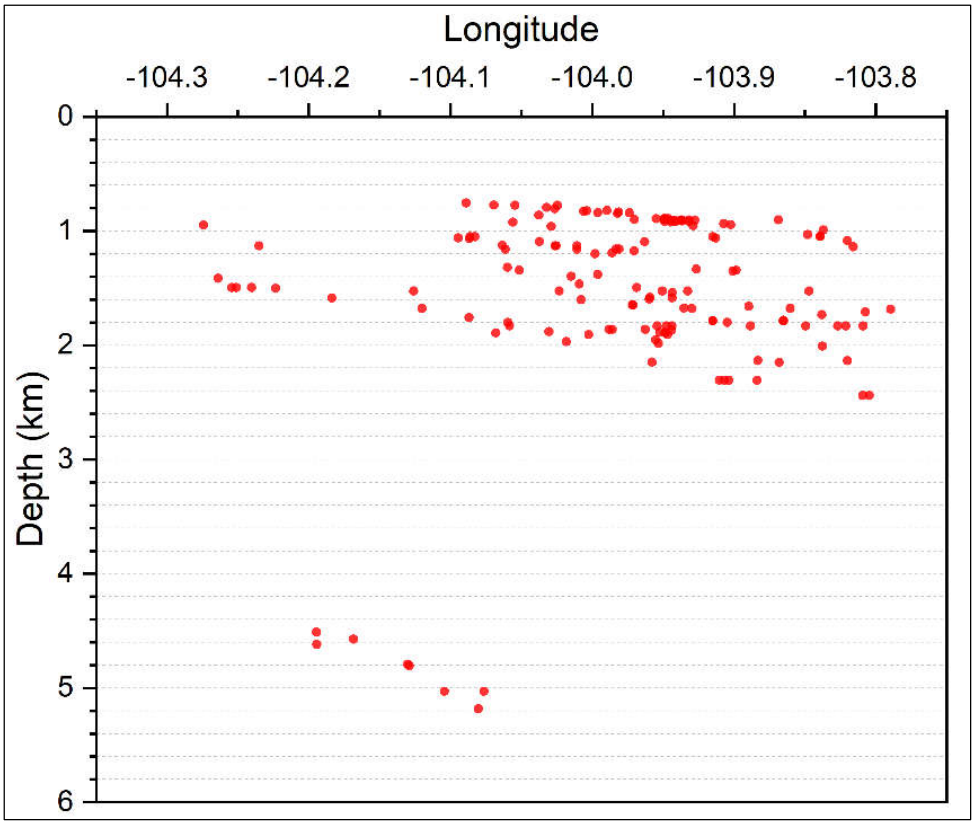

Figure S3. Distribution of well bottom depth.

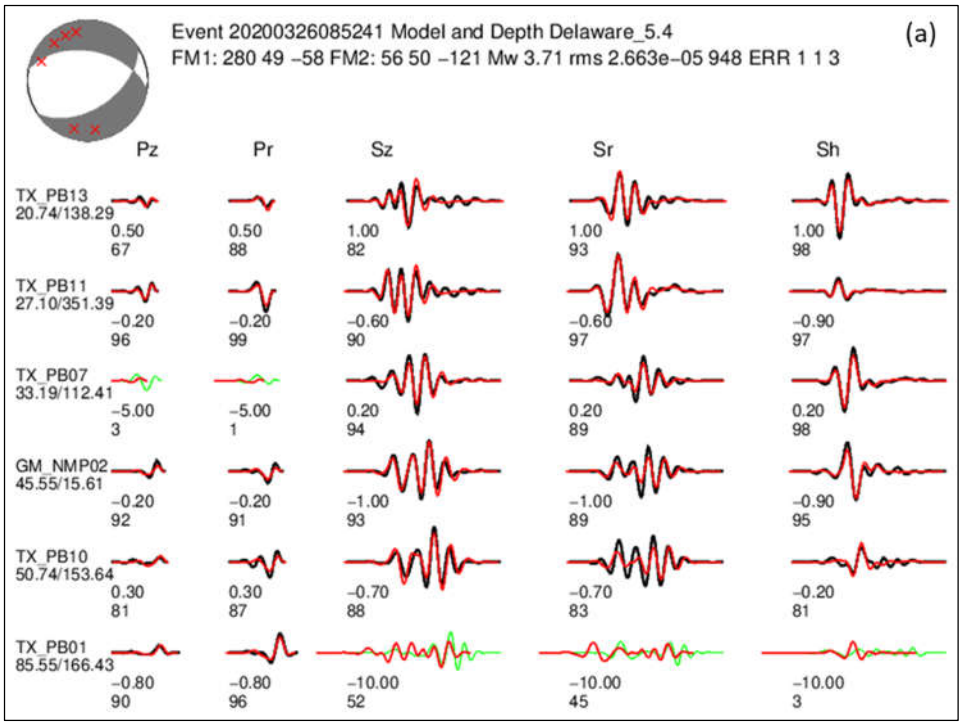

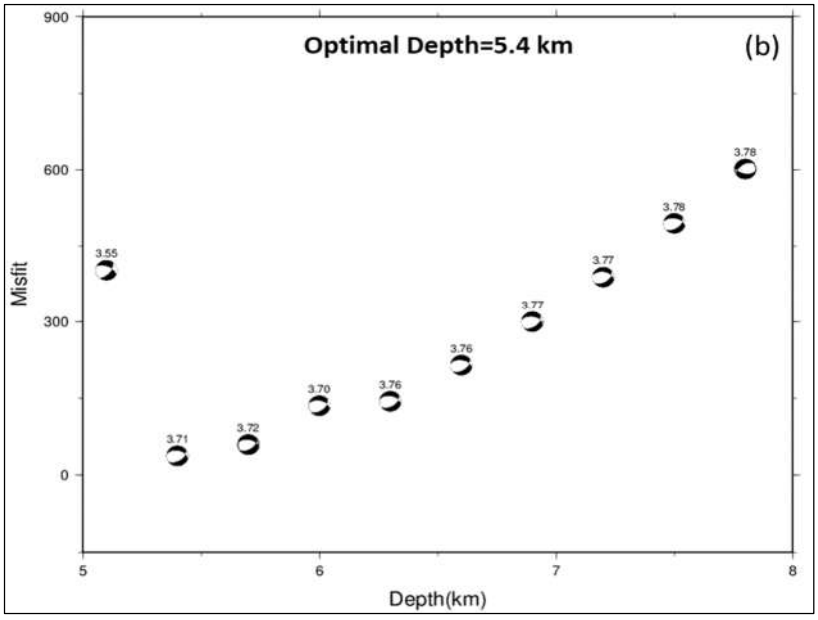

Figure S4. (a) Cross correlation (cc) of synthetic (red) and actual (black) waveforms at the optimal depth of event 02. Green waveforms are below the cc threshold and not accounted for in inversion results. The numbers below the waveforms are optimal shift time (in second) and cross correlation, respectively. (b) Relative misfit error of event 02 inversion at different focal depths.

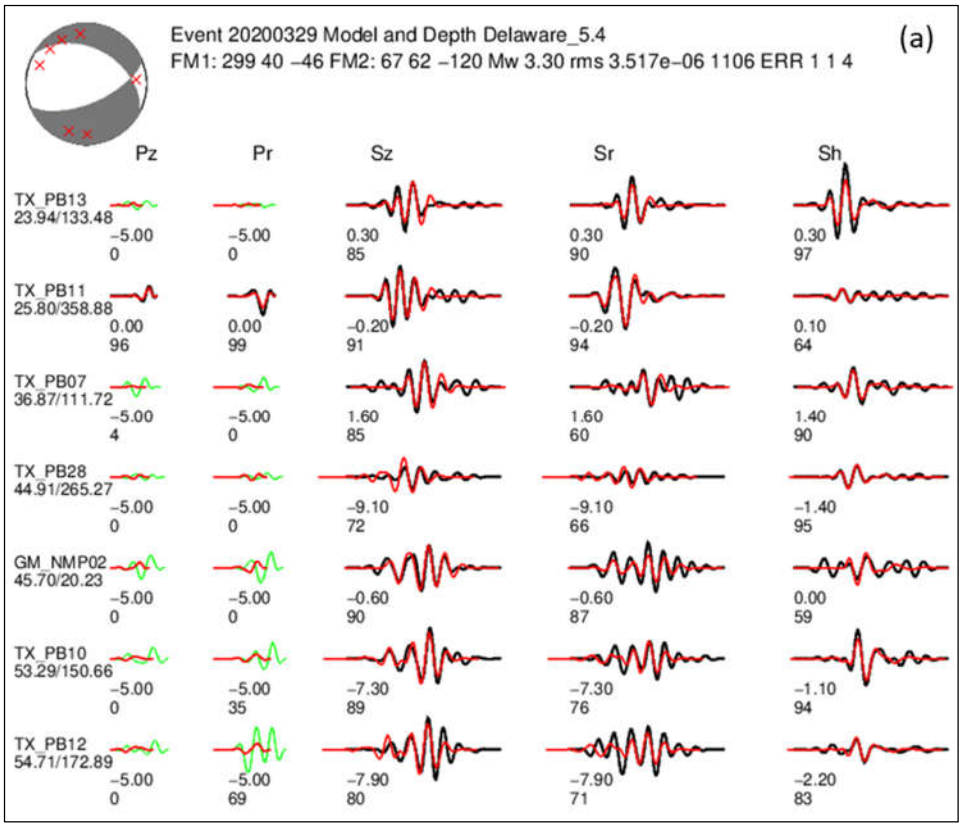

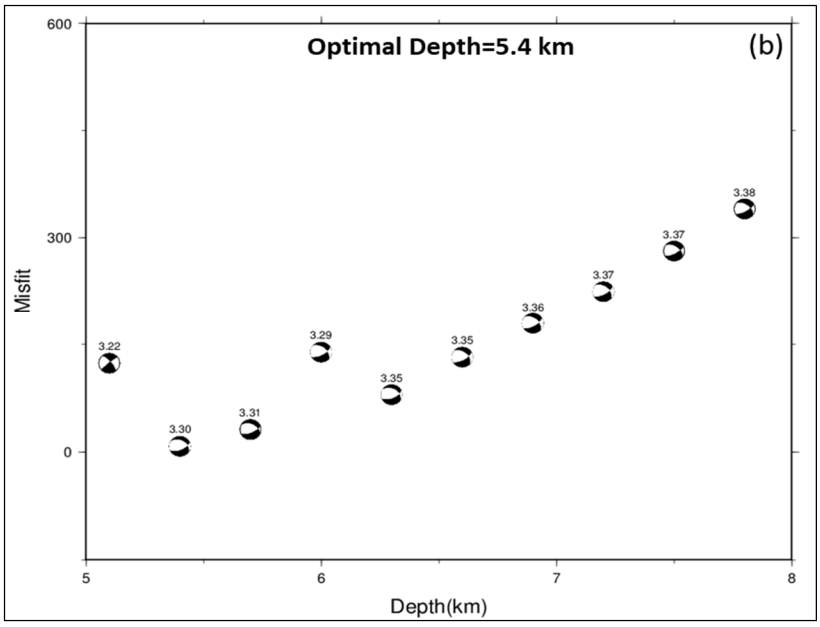

Figure S5. (a) Cross correlation (cc) of synthetic (red) and actual (black) waveforms at the optimal depth of event 03. Green waveforms are below the cc threshold and not accounted for in inversion results. The numbers below the waveforms are optimal shift time (in second) and cross correlation, respectively. (b) Relative misfit error of event 03 inversion at different focal depths.

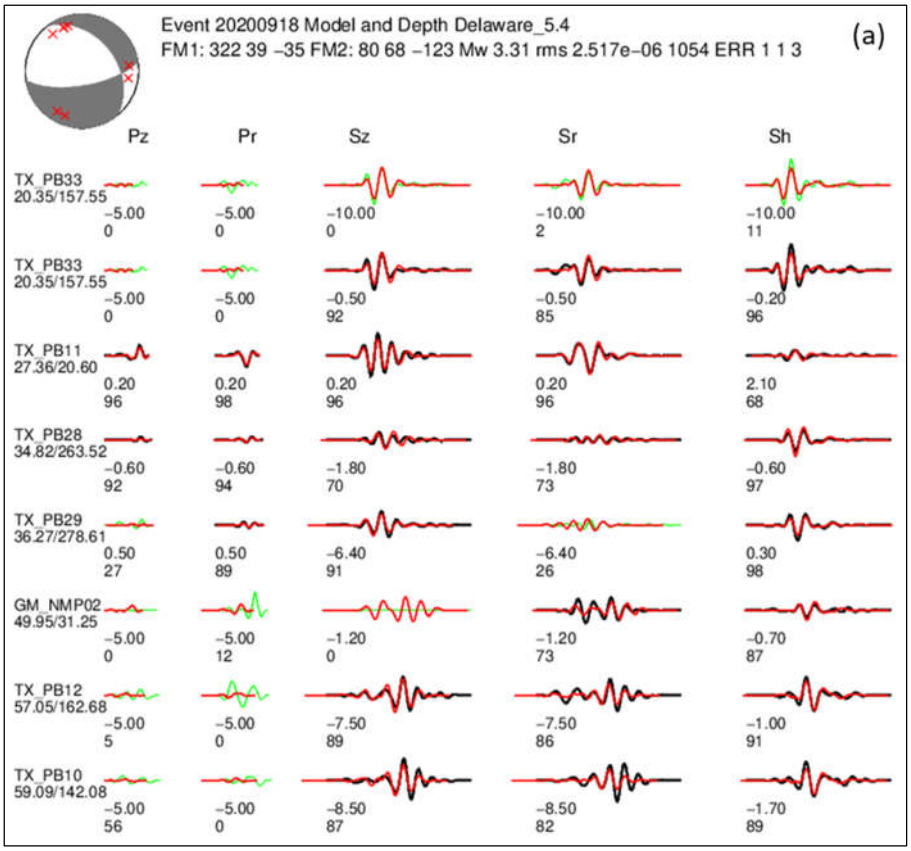

45

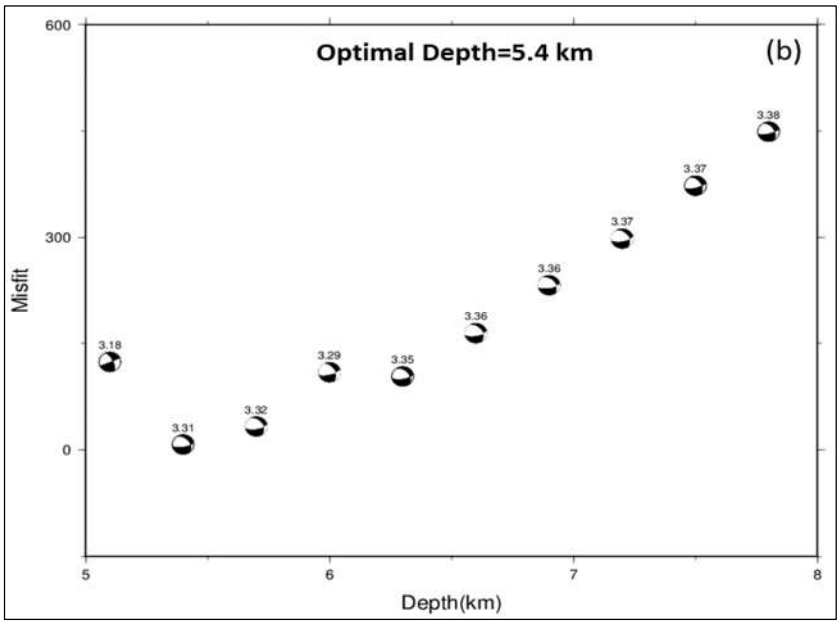

46

47 **Figure S6.** (a) Cross correlation (cc) of synthetic (red) and actual (black) waveforms at the
48 optimal depth of event 04. Green waveforms are below the cc threshold and not
49 accounted for in inversion results. The numbers below the waveforms are optimal shift
50 time (in second) and cross correlation, respectively. (b) Relative misfit error of event 04
51 inversion at different focal depths.

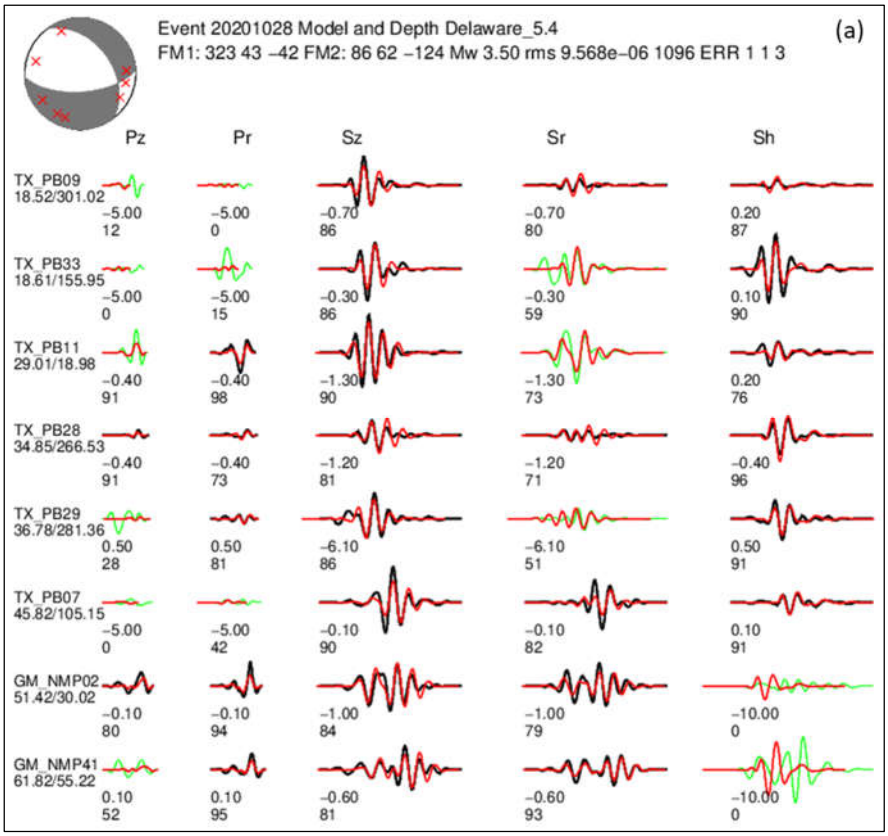

52

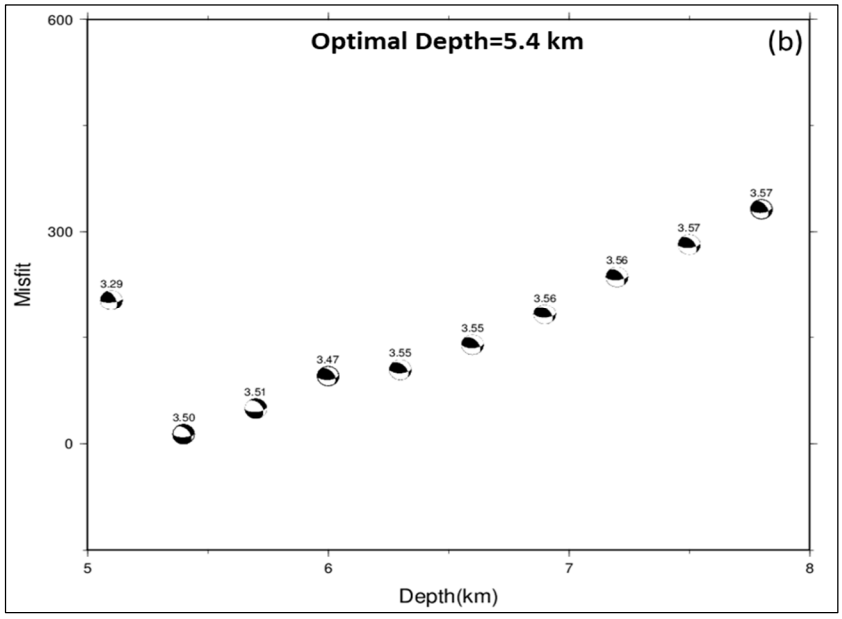

53

54 **Figure S7.** (a) Cross correlation (cc) of synthetic (red) and actual (black) waveforms at the
55 optimal depth of event 05. Green waveforms are below the cc threshold and not
56 accounted for in inversion results. The numbers below the waveforms are optimal shift
57 time (in second) and cross correlation, respectively. (b) Relative misfit error of event 05
58 inversion at different focal depths.

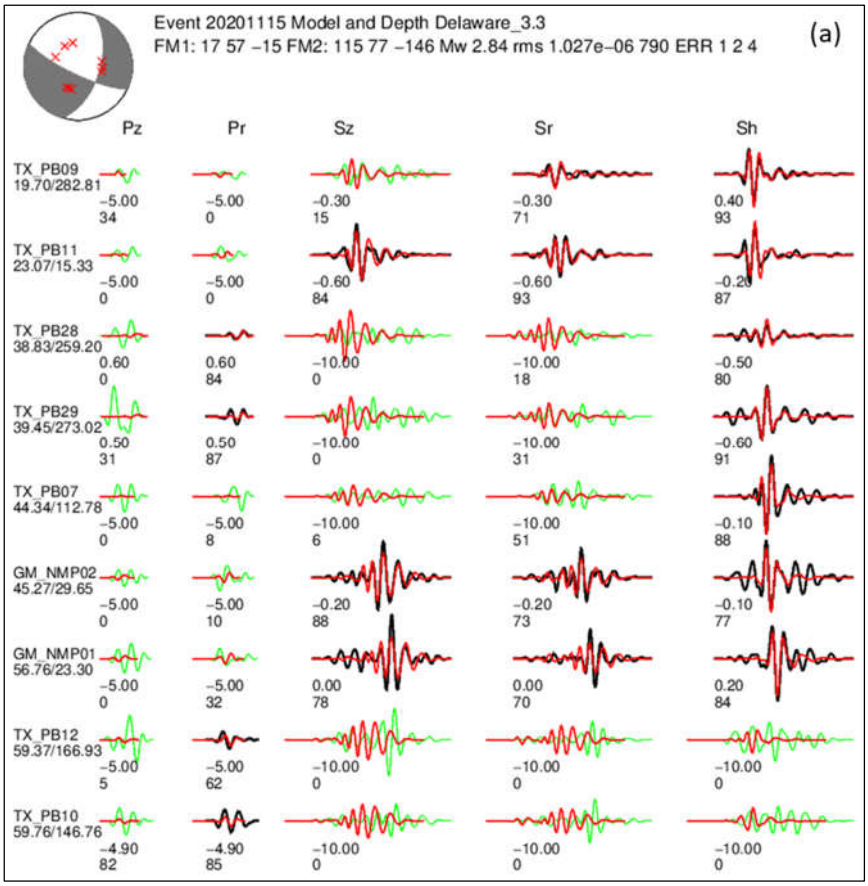

59

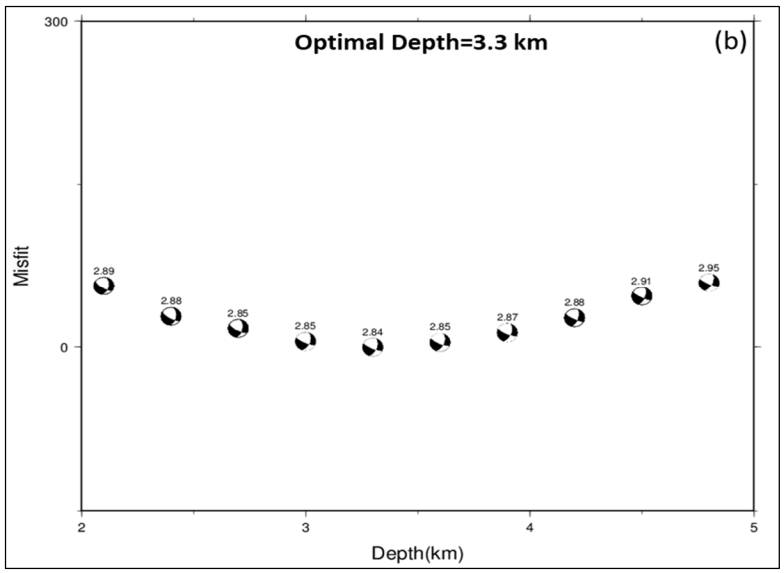

60

61 **Figure S8.** (a) Cross correlation (cc) of synthetic (red) and actual (black) waveforms at the
62 optimal depth of event 06. Green waveforms are below the cc threshold and not
63 accounted for in inversion results. The numbers below the waveforms are optimal shift
64 time (in second) and cross correlation, respectively. (b) Relative misfit error of event 06
65 inversion at different focal depths.

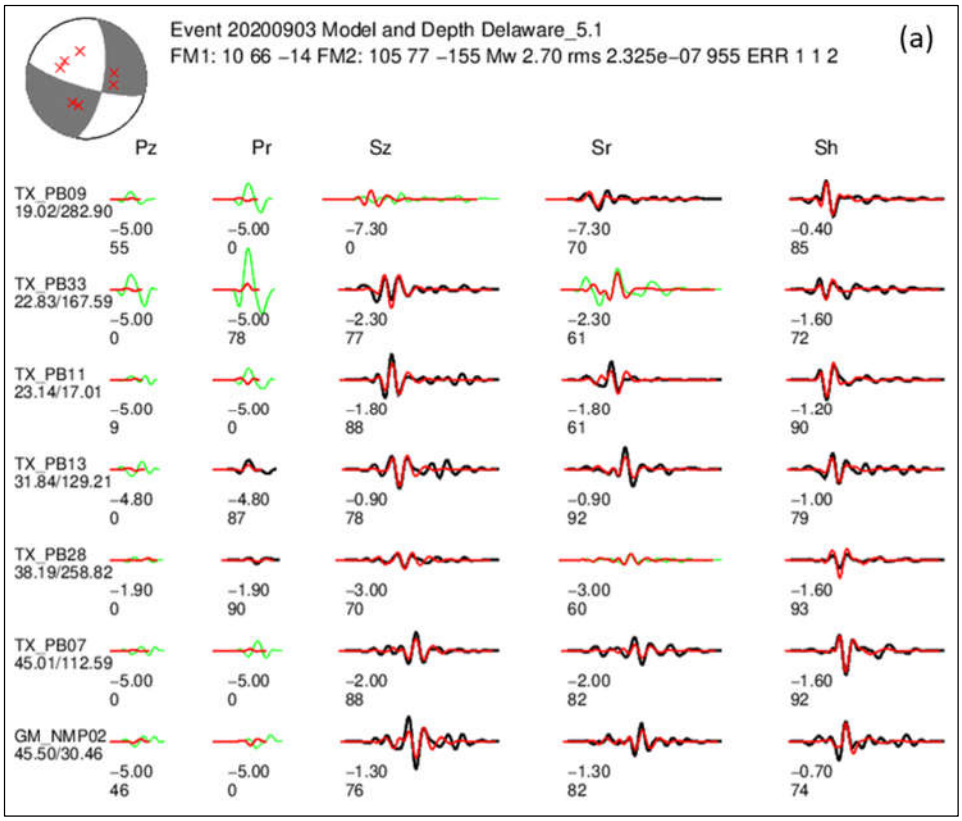

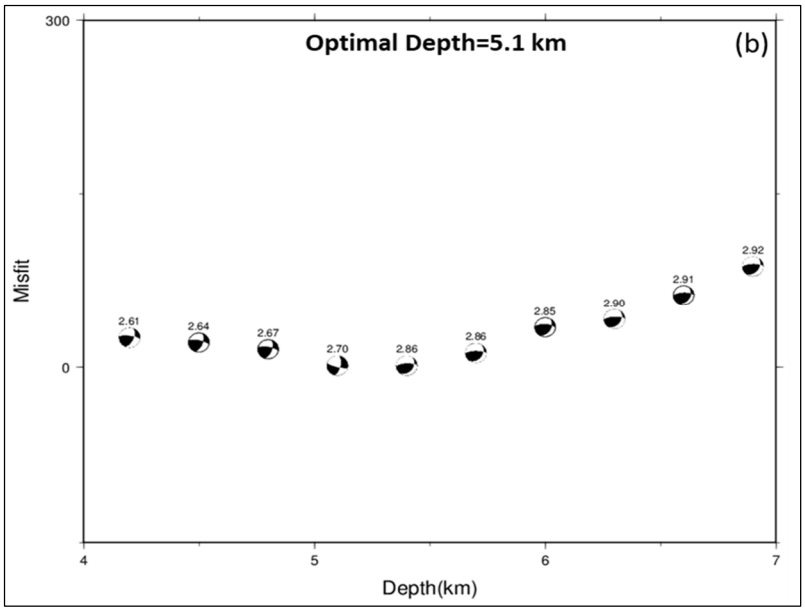

Figure S9. (a) Cross correlation (cc) of synthetic (red) and actual (black) waveforms at the optimal depth of event 07. Green waveforms are below the cc threshold and not accounted for in inversion results. The numbers below the waveforms are optimal shift time (in second) and cross correlation, respectively. (b) Relative misfit error of event 07 inversion at different focal depths.

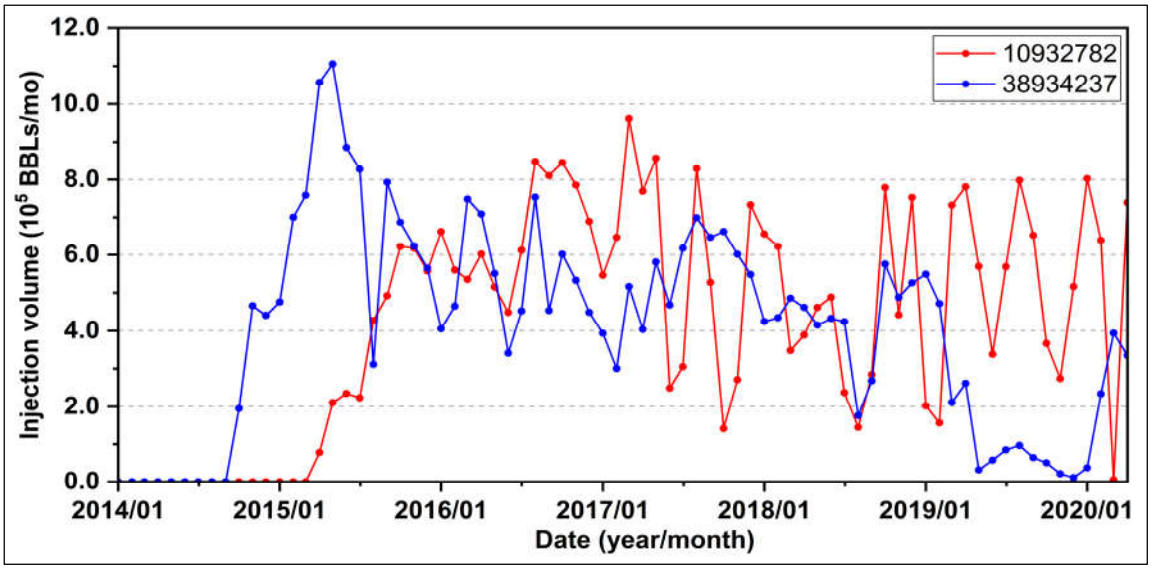

Figure S10. Monthly injection rate of selected shallow and deep injection wells (horizontal axis starts from 2014 since these two wells have no injection activity before 2014).

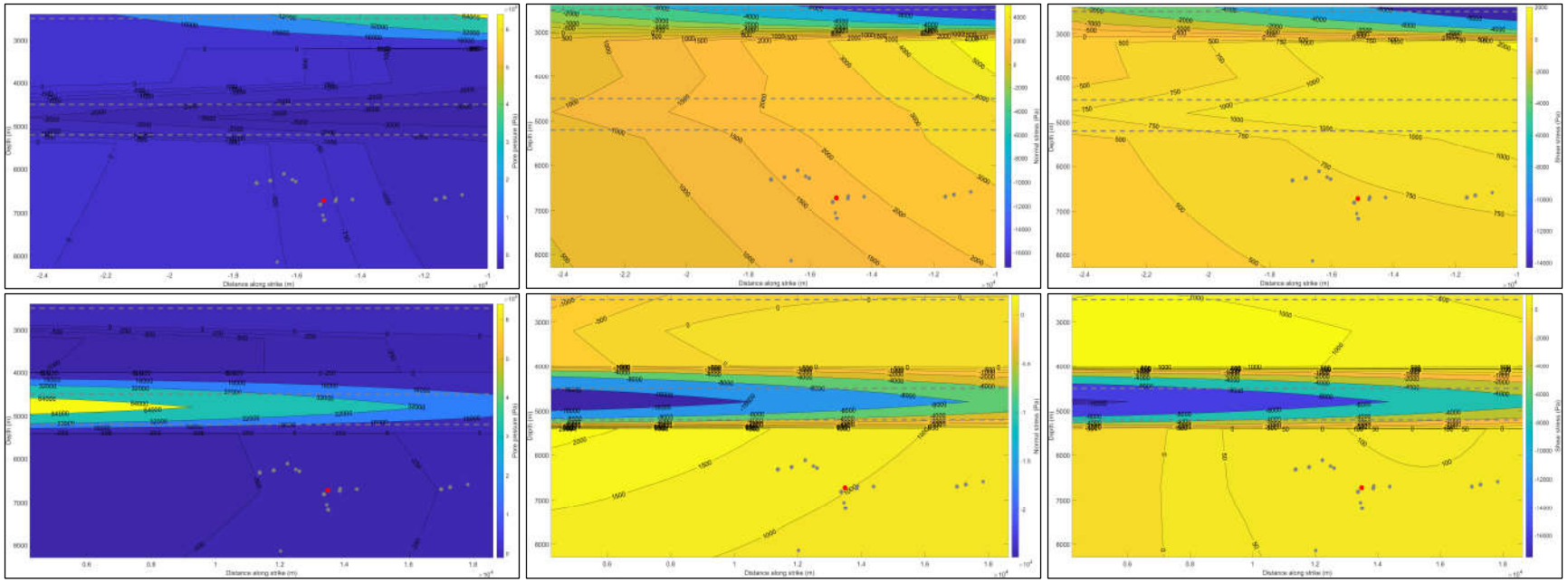

Figure S11. Resulted pore pressure, normal stress and shear stress of selected shallow and deep injection wells (Top row: shallow injection well, bottom row: deep injection well. From left to right: Pore pressure, normal stress, shear stress.) The gray dashed lines separate the sandstone, shale, limestone and basement layers (from top to bottom).

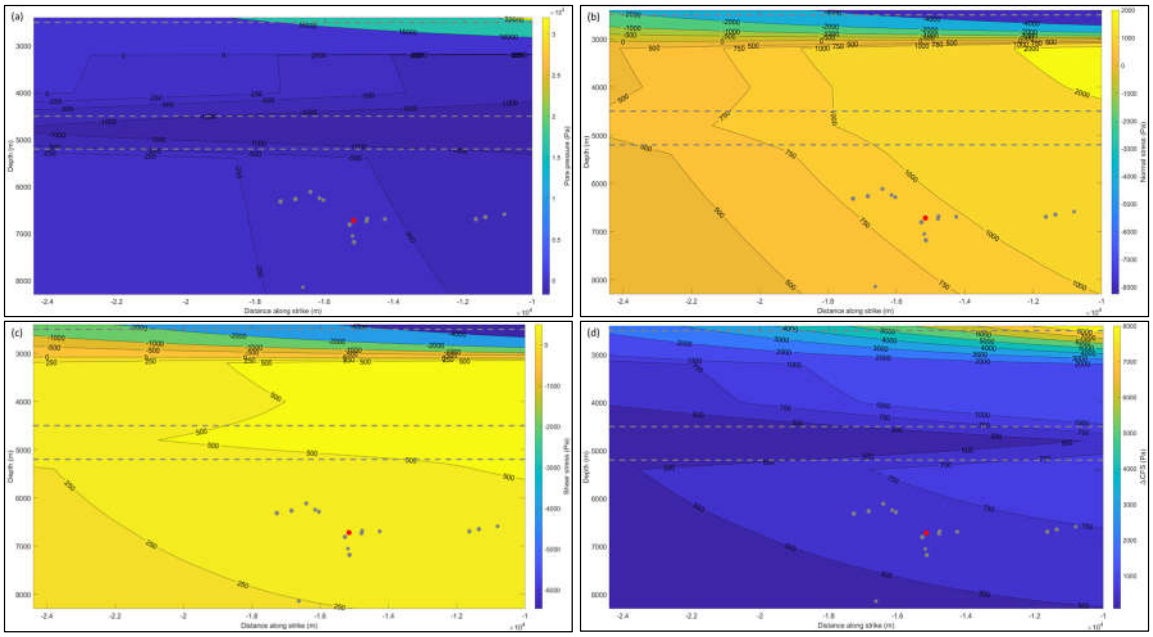

Figure S12. Resulted (a) pore pressure, (b) normal stress, (c) shear stress and (d) ΔCFS of shallow injection scenario SI-2. The gray dashed lines separate the sandstone, shale, limestone and basement layers (from top to bottom).

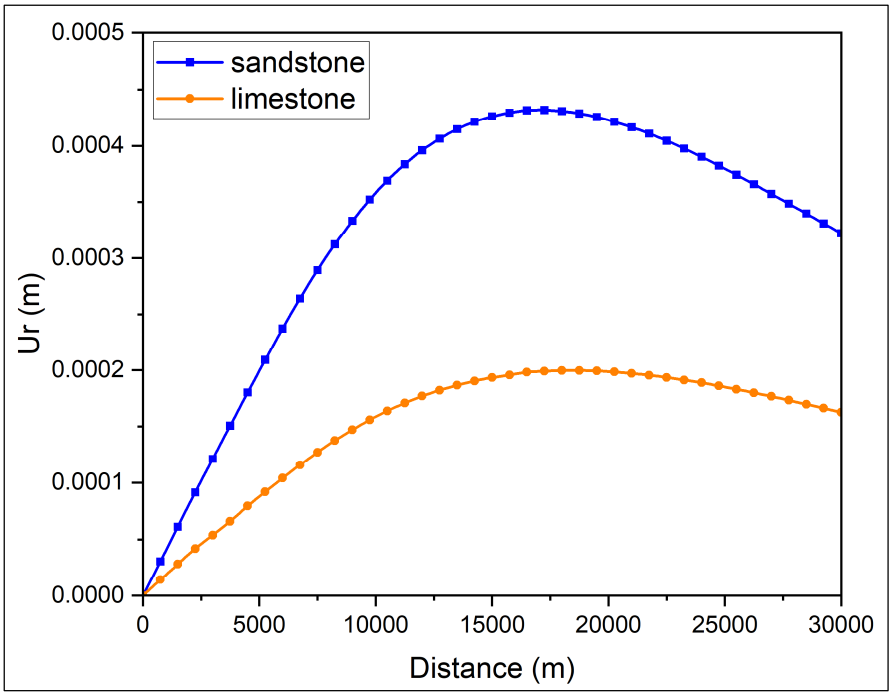

87

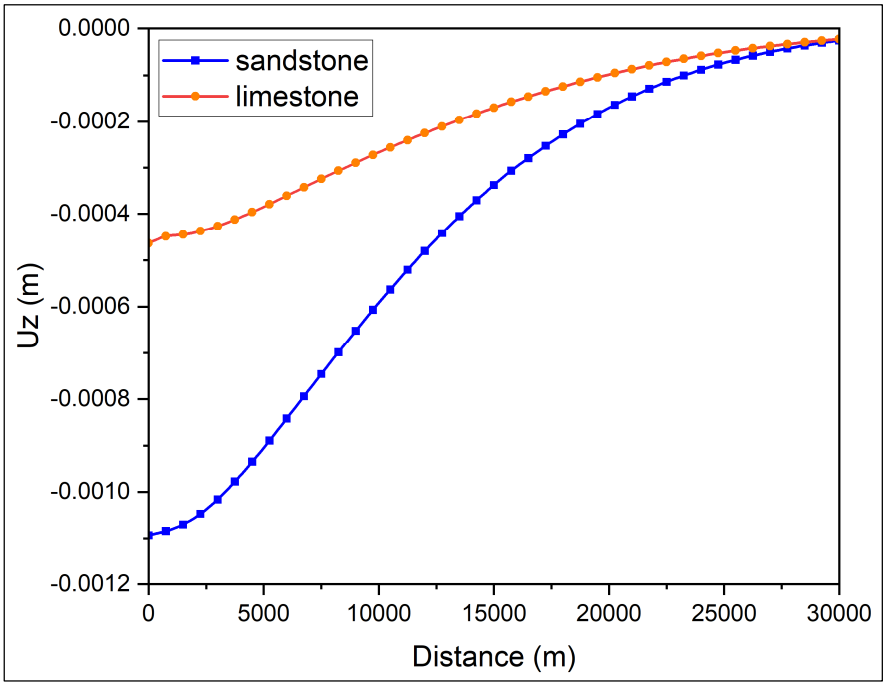

88

89 **Figure S13.** Simulated poroelastic deformation in the r and z direction within the
90 basement layer where the mainshock occurred (depth = 6.7 km) as a result of shallow
91 injections in scenario SI-1 (sandstone layer) and SI-2 (limestone layer), respectively.

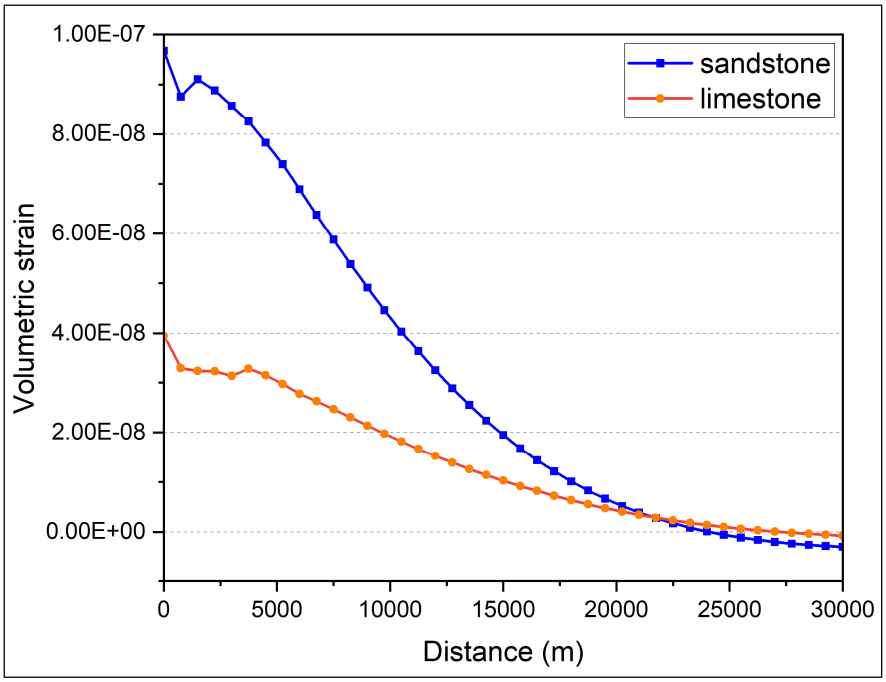

92

93 **Figure S14.** Resulted volumetric strain in scenarios SI-1 (sandstone layer) and SI-2
94 (limestone layer) within the mainshock layer (depth = 6.7 km).

MINWGHT	MAXDIST	MAXSEP	MAXNGH	MINLINK	MINOBS	MAXOBS
0	400	6	8	8	1	50

NITER	WTCCP	WTCCS	WRCC	WDCC	WTCTP	WTCTS	WRCT	WDCT	DAMP
5	0.01	0.01	-9	-9	1.0	0.5	-9	-9	40
5	1	0.5	-9	6	0.001	0.001	-9	5	40
5	1	0.5	-9	5	0.001	0.001	6	5	40
5	1	0.5	6	5	0.001	0.001	6	5	40
5	1	0.5	6	3	0.001	0.001	6	3	40

Table S1. Input parameters used in hypoDD. (MINWGHT: minimum pick weight allowed, MAXDIST: maximum distance in km between event pair and stations, MAXSEP: maximum hypocentral separation in km, MAXNGH: maximum number of neighbors per event, MINLINK: minimum number of links required to define a neighbor, MINOBS: minimum number of links per pair saved, MAXOBS: maximum number of links per pair saved, NITER: number of iterations used for listed weights, WTCCP and WTCCS: weight of cross P wave and S wave, WRCC and WRCT: residual threshold in seconds for cross and catalog data, WTCTP and WTCTS: weight of catalog P wave and S wave, WDCC and WDCT: maximum distance (km) between cross and catalog linked pairs, DAMP: damping parameters used in iteration.

Quadrant	Calculation groups	API number	Total injection volume (BBLS)	Pore pressure (Pa)	Normal stress (Pa)	Shear stress (Pa)	ΔCFS (Pa)
NW	1_1	10932849	26262354	-242.34	1296.89	679.02	1311.75
	1_2	10932848	25035604	15.45	856.22	504.38	1027.39
	1_2	10933282	20785411	224.65	570.81	445.01	922.29
	1_2	10933281	9331550	157.77	226.58	187.73	418.34
	2	10931638	4004484	-80.93	201.30	3.03	75.25
	2	10931565	2063288	-31.14	104.14	-7.20	36.60
SE	1	38934609	42808426	67.62	301.05	1760.19	1981.39
	1	38935413	17916180	159.88	8.76	817.77	918.96
	2	38933269	29133703	-194.99	-174.64	1470.67	1248.89
	2	38936297	14006303	189.88	-468.49	905.93	738.76
	3	38935362	17475621	-991.47	114.86	1509.88	983.91
SW	1	10933058	14768626	-2416.70	2107.91	1022.17	836.90
	2	10932340	10615573	-1257.32	1375.22	605.03	675.77
	3	10933071	7493206	9.28	-522.20	57.38	-250.37
	4	38934925	6382062	-307.22	3.38	157.87	-24.44
NE	1_1	38934274	56124718	-710.67	2867.34	1319.81	2613.81
	1_1	38934372	5884046	-136.54	314.06	121.39	227.90
	1_1	38933271	9924847	-288.00	584.40	212.41	390.25
	1_2	38934237	30472454	-693.94	1717.80	694.96	1309.28
	1_2	38934942	27914073	-183.61	1370.55	708.66	1420.82
	1_2	38934935	3625343	-26.56	182.75	86.83	180.55
	2	38934929	36359171	153.11	1083.01	418.75	1160.43
	2	38935968	15547400	254.52	346.41	125.04	485.59
	3	38934661	29089012	100.21	640.10	-301.16	143.03
	3	38935357	21147125	219.13	334.57	-316.80	15.42
	4	38933299	15751034	30.48	213.40	-220.80	-74.47
	4	38935108	7248901	80.71	16.52	-161.79	-103.45
	4	38933620	10914961	41.78	118.30	-175.90	-79.85
	4	38933298	10573269	-30.37	207.29	-97.95	8.21
	5	38932872	11751801	-175.25	494.39	65.20	256.69
	5	38936030	8596403	81.58	222.87	-38.02	144.65
	5	38936032	3146446	77.94	51.70	-66.47	11.31
	6	38935886	14115239	235.58	32.50	-345.34	-184.49
	6	38936478	8264986	147.98	-2.05	-234.14	-146.58
	7	38935373	20599155	231.10	73.69	-427.02	-244.15
	8	38932527	6148354	-181.16	456.70	135.46	300.79
	8	38932506	4547952	-113.57	324.94	101.29	228.11
	8	38932507	3713541	-81.21	261.39	85.04	193.15
	8	38932528	2602393	-87.25	201.70	59.04	127.70

Table S2. Information of selected wells and resulted pore pressure, normal stress, shear stress and ΔCFS from POEL modeling. (Total injection volume is from xx, 20xx to April 2020).

API	UIC number	Injection depth (m)	Latitude	Longitude	Total injection volume (BBLS)
38934237	000108878	2305	31.825	-103.90695815	30472454
10932782	000111641	4800	31.81591	-104.1945797	31218221

Table S3. Information of selected shallow and deep injection well.